

RESEARCH ARTICLE | AUGUST 30 2024

# A stochastic Schrödinger equation and matrix product state approach to carrier transport in organic semiconductors with nonlocal electron–phonon interaction

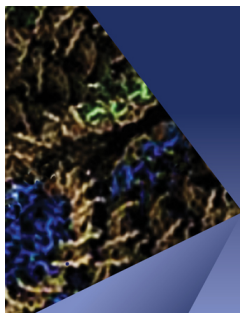
Special Collection: [Algorithms and Software for Open Quantum System Dynamics](#)

Liqi Zhou ; Xing Gao  ; Zhigang Shuai  



*J. Chem. Phys.* 161, 084118 (2024)

<https://doi.org/10.1063/5.0221143>



The Journal of  
Chemical Physics

Special Topic:

Chromatin Structure and Dynamics:  
Recent Advancements

[Submit Today!](#)

# A stochastic Schrödinger equation and matrix product state approach to carrier transport in organic semiconductors with nonlocal electron–phonon interaction

Cite as: *J. Chem. Phys.* **161**, 084118 (2024); doi: [10.1063/5.0221143](https://doi.org/10.1063/5.0221143)

Submitted: 30 May 2024 • Accepted: 12 August 2024 •

Published Online: 30 August 2024



View Online



Export Citation



CrossMark

Liqi Zhou,<sup>1</sup>  Xing Gao,<sup>2,a)</sup>  and Zhigang Shuai<sup>1,3,a)</sup> 

## AFFILIATIONS

<sup>1</sup>MOE Key Laboratory of Organic OptoElectronics and Molecular Engineering, Department of Chemistry, Tsinghua University, Beijing 100084, China

<sup>2</sup>School of Materials, Sun Yat-sen University, Shenzhen, Guangdong 518107, China

<sup>3</sup>School of Science and Engineering, The Chinese University of Hong Kong, Shenzhen, Guangdong 518172, China

**Note:** This paper is part of the JCP Special Topic on Algorithms and Software for Open Quantum System Dynamics.

<sup>a)</sup>Authors to whom correspondence should be addressed: [gxing@mail.sysu.edu.cn](mailto:gxing@mail.sysu.edu.cn) and [shuaizhigang@cuhk.edu.cn](mailto:shuaizhigang@cuhk.edu.cn)

## ABSTRACT

Evaluation of the charge transport property of organic semiconductors requires exact quantum dynamics simulation of large systems. We present a numerically nearly exact approach to investigate carrier transport dynamics in organic semiconductors by extending the non-Markovian stochastic Schrödinger equation with complex frequency modes to a forward–backward scheme and by solving it using the matrix product state (MPS) approach. By utilizing the forward–backward formalism for noise generation, the bath correlation function can be effectively treated as a temperature-independent imaginary part, enabling a more accurate decomposition with fewer complex frequency modes. Using this approach, we study the carrier transport and mobility in the one-dimensional Peierls model, where the nonlocal electron–phonon interaction is taken into account. The reliability of this approach was validated by comparing carrier diffusion motion with those obtained from the hierarchical equations of motion method across various parameter regimes of the phonon bath. The efficiency was demonstrated by the modest virtual bond dimensions of MPS and the low scaling of the computational time with the system size.

Published under an exclusive license by AIP Publishing. <https://doi.org/10.1063/5.0221143>

## I. INTRODUCTION

Carrier mobility is a critical parameter for assessing the charge transport property of organic semiconductors, which poses challenges to theoretical research due to the complexity with the flexible and disordered backbone structure.<sup>1,2</sup> Numerous mechanisms have been proposed to understand carrier dynamics, including “band-like” behavior,<sup>3–5</sup> hopping transport,<sup>6,7</sup> phonon-assisted transport,<sup>8,9</sup> and transition localization,<sup>10,11</sup> each of which could be found applicability in organic materials with specific ranges of charge transfer integral and electron–phonon interaction, respectively.<sup>12,13</sup> Numerically exact methods, such as the

time-dependent density matrix renormalization group (TD-DMRG) approach, which is effective for studying both local and nonlocal electron–phonon interactions, can provide a comprehensive understanding of the charge transport mechanisms.<sup>14,15</sup> However, the exact treatment of all phonon modes may limit its applicability to the large systems required for simulating charge diffusive motion. This limitation highlights the need for more efficient methods to accurately address electron–phonon interactions.

Alternatively, open quantum system methods,<sup>16</sup> which focus solely on reduced dynamics by tracing out the bath degrees of freedom of phonons, offered a promising approach for such a purpose. To accurately describe carrier dynamics, it is essential to

account for the memory effects from the bath (non-Markovian effects<sup>17</sup>) across various coupling strengths to the bath due to the comparative timescales of electron transfer process and vibration relaxation.<sup>18</sup>

Various methods based on reduced density matrix, such as the quasi-adiabatic path integral (QUAPI),<sup>19,20</sup> the hierarchical equations of motion (HEOM),<sup>21,22</sup> and the Nakajima–Zwanzig equation,<sup>23,24</sup> were proposed to handle non-Markovian dynamics accurately and have been extensively applied to investigate carrier transport processes in organic semiconductors.<sup>25–29</sup> Unlike deterministic methods, stochastic methods are another class of approaches for open quantum systems, including the density-operator-based stochastic Liouville equations (SLEs)<sup>30–34</sup> and stochastic HEOM methods,<sup>35</sup> as well as the wave-function-based stochastic Schrödinger equations (SSEs).<sup>36–38</sup> As an unraveling of density matrix evolution, SSE methods produce results by averaging over multiple trajectories of stochastic wave functions, offering lower space complexity and facilitating parallel computation. The time-dependent wave packet diffusion (TDWPD) method, a typical SSE approach, has been utilized to simulate the charge transport process in hundreds or even thousands of sites.<sup>39–41</sup> However, it cannot fully describe the low-temperature dynamics due to the neglect of the imaginary part of the bath correlation function (BCF).<sup>39</sup> The non-Markovian stochastic Schrödinger equation (NMSSE) presents a numerically exact method, albeit with the challenge of implementing its complex functional derivative term with respect to the noise.<sup>36,37</sup> To address this problem without compromising accuracy, the hierarchy of pure states (HOPS) method was proposed by introducing auxiliary stochastic wave functions and constructing hierarchical equations.<sup>42</sup> Different noise generation schemes, including the forward–backward formalism, have been developed to enhance applicability across different temperature regimes and spectral densities,<sup>43–46</sup> as well as to reduce the number of auxiliary wave functions in HOPS. Both NMSSE and HOPS have exhibited the potential to evaluate the spectra or charge transport properties of organic materials.<sup>43,47,48</sup> In addition, leveraging the localized nature of charge carriers, the recently developed adaptive HOPS (adHOPS) method with size-invariant scaling demonstrates advantages in quantum simulation of large systems.<sup>49–51</sup>

The advancement of tensor network states (TNS), a low-entanglement representation of many-body states, can significantly reduce the computational cost for simulating quantum dynamics.<sup>52–54</sup> TNS formalism has been integrated with various open quantum system methods, including propagating the influence functional directly<sup>55–58</sup> or solving equations of motion,<sup>59–64</sup> to simulate the dynamic evolution of the reduced density matrix. In our previous work, we reformulated the HOPS using conventional ladder operators in Fock space and wave function rescaling techniques to derive a NMSSE in complex frequency modes (cNMSSE). We subsequently solved the cNMSSE using the matrix product state (MPS) method to simulate exciton diffusion dynamics in a linear chain, considering local electron–phonon interactions at zero

temperature.<sup>63</sup> However, we overlooked scenarios involving non-local electron–phonon interaction, which is relevant for charge transport as shown in other studies conducted within mixed quantum/classical dynamics,<sup>65–67</sup> polaron transformation,<sup>8,68</sup> or transient localization theory.<sup>10,11</sup>

In this work, we extend the cNMSSE method to the forward–backward formalism,<sup>45,46</sup> which results in an adjusted bath correlation function that only contains the temperature-independent imaginary part and can be decomposed into fewer modes with greater accuracy. We employ this method to investigate the diffusion dynamics of a single charge carrier within the one-dimensional Peierls model with nonlocal electron–phonon coupling. The accuracy of the cNMSSE method was validated by benchmarking against the HEOM method, and its computational efficiency was assessed by analyzing the computational cost of individual trajectories and the convergence trend of averaged trajectories. Our computations are executed using Renormalizer, a home-made python package designed for quantum dynamics simulation based on the TD-DMRG method (Appendix A).<sup>69,70</sup>

## II. METHODS

### A. Non-Markovian stochastic Schrödinger equation

We begin with the Hamiltonian of a quantum system coupled linearly with a bosonic bath,

$$\begin{aligned} \hat{H} &= \hat{H}_S + \hat{H}_B + \hat{H}_{SB} \\ &= \hat{H}_S + \sum_{\lambda} \left( \frac{\hat{p}_{\lambda}^2}{2m_{\lambda}} + \frac{1}{2} m_{\lambda} \omega_{\lambda}^2 \hat{x}_{\lambda}^2 \right) + \hat{f}(q) \otimes \hat{B}, \end{aligned} \quad (1)$$

where  $\hat{H}_S$  is the system Hamiltonian and  $\hat{H}_B$  describes the bath composed of identical harmonic oscillators. The third term illustrates the linear coupling between the system operator  $\hat{f}(q)$  and the collective bath coordinate  $\hat{B} = \sum_{\lambda} c_{\lambda} \hat{x}_{\lambda}$ .

Initially, it is assumed that there is no interaction between the system and the bath, and the bath remains in thermal equilibrium. Therefore, the total initial density matrix can be written as a tensor product of the system and bath density matrices:  $\rho_{\text{tot}}(0) = \rho_S(0) \otimes \rho_B$ . Here,  $\rho_B$  is given by the thermal equilibrium state  $\rho_B = \frac{e^{-\beta \hat{H}_B}}{\text{Tr}\{e^{-\beta \hat{H}_B}\}}$ , where  $\beta$  is inverse temperature (we use the units  $\hbar = k_B = 1$  throughout this section). To exactly describe the evolution of the reduced density matrix of system, we employed a double path integral formalism.<sup>71</sup> The reduced density matrix  $\rho_S(t)$  at time  $t$  is given by

$$\rho_S(t) = \int \mathcal{D}[q^+] \int \mathcal{D}[q^-] e^{iS_0[q^+]} \rho_S(0) e^{-iS_0[q^-]} \mathcal{F}[q^+, q^-, t], \quad (2)$$

where  $S_0[q^+]$  and  $S_0[q^-]$  are actions defined by  $\hat{H}_S$  on forward path  $q^+$  and backward path  $q^-$ , respectively, and  $\mathcal{F}[q^+, q^-, t]$  represents the Feynman–Vernon influence functional,

$$\mathcal{F}[q^+, q^-, t] = \exp \left\{ - \int_0^t ds \int_0^s du \left( f(q^+(s)) f(q^-(s)) \begin{pmatrix} \alpha(s, u) & -\alpha^*(s, u) \\ -\alpha(s, u) & \alpha^*(s, u) \end{pmatrix} \begin{pmatrix} f(q^+(u)) \\ f(q^-(u)) \end{pmatrix} \right) \right\}. \quad (3)$$

Here, the bath correlation function (BCF) indicates the bath memory (non-Markovianity),

$$\alpha(t, s) = \text{Tr}\{\hat{B}(t)\hat{B}(s)\rho_B\} = \int_0^\infty \frac{d\omega}{\pi} J(\omega) \times \left[ \coth \frac{\beta\omega}{2} \cos \omega(t-s) - i \sin \omega(t-s) \right], \quad (4)$$

where

$$J(\omega) = \frac{\pi}{2} \sum_\lambda \frac{c_\lambda^2}{\omega_\lambda} \delta(\omega - \omega_\lambda) \quad (5)$$

is the spectral density that implies the interaction intensity between the system and different bath modes. The non-Markovian effects matter when the BCF decays to zero slowly compared with the relaxation of the system. The off-diagonal kernel matrix of the influence

functional indicates the coupling between the forward and backward paths and can be divided into the diagonal and off-diagonal components,

$$\begin{pmatrix} \alpha(s, u) & -\alpha^*(s, u) \\ -\alpha(s, u) & \alpha^*(s, u) \end{pmatrix} = \begin{pmatrix} \tilde{\alpha}(s, u) & 0 \\ 0 & \tilde{\alpha}^*(s, u) \end{pmatrix} + \begin{pmatrix} \alpha(s, u) - \tilde{\alpha}(s, u) & -\alpha^*(s, u) \\ -\alpha(s, u) & \alpha^*(s, u) - \tilde{\alpha}^*(s, u) \end{pmatrix}, \quad (6)$$

where  $\tilde{\alpha}(s, u)$  is the adjusted BCF (aBCF) that will be explained later. The Hubbard–Stratonovich (H–S) transformation is used to further decouple the forward and backward paths at the cost of introducing stochastic noises,<sup>72</sup>

$$\begin{aligned} & \mathcal{E} \left\{ \exp \left[ -i \int_0^t ds (Z_+(s)f(q^+(s)) - Z_-^*(s)f(q^-(s))) \right] \right\}_z \\ &= \exp \left\{ - \int_0^t ds \int_0^s du (f(q^+(s)) \quad f(q^-(s))) \begin{pmatrix} \alpha_1(s, u) & -\alpha_2(s, u) \\ -\alpha_2^*(s, u) & \alpha_1^*(s, u) \end{pmatrix} \begin{pmatrix} f(q^+(u)) \\ f(q^-(u)) \end{pmatrix} \right\}, \quad (7) \end{aligned}$$

where  $\alpha_1$  and  $\alpha_2$  are correlation functions of the complex Gaussian noises  $Z_\pm$ ,

$$\mathcal{E}\{Z_+(s)\}_z = \mathcal{E}\{Z_-(s)\}_z = 0, \quad (8)$$

$$\mathcal{E}\{Z_+(s)Z_+(u)\}_z = \mathcal{E}\{Z_-(s)Z_-(u)\}_z = \alpha_1(s, u) = \alpha(s, u) - \tilde{\alpha}(s, u), \quad (9)$$

$$\mathcal{E}\{Z_+(s)Z_-^*(u)\}_z = \alpha_2(s, u) = \alpha^*(s, u). \quad (10)$$

The  $\mathcal{E}\{\dots\}_z$  denotes the stochastic average over Gaussian noises. The derivation of the H–S transformation is detailed in [Appendix B](#). Equation (10) ensures the decoupling of the forward and backward paths in the influence functional, while the selection of  $\alpha_1$  in Eq. (9) is flexible with different noise generation schemes. According to Eq. (6), the influence functional can then be divided into two parts,

$$\begin{aligned} \mathcal{F}[q^+, q^-, t] &= \exp(-\Phi_{\text{res}}[q^+, t] - \Phi_{\text{res}}^*[q^-, t]) \mathcal{E} \\ &\times \left\{ \exp \left[ -i \int_0^t ds (Z_+(s)f(q^+(s)) \right. \right. \\ &\quad \left. \left. - Z_-^*(s)f(q^-(s))) \right] \right\}_z, \quad (11) \end{aligned}$$

where

$$\Phi_{\text{res}}[q^\pm, t] = \int_0^t ds \int_0^s du f(q^\pm(s)) \tilde{\alpha}(s, u) f(q^\pm(u)). \quad (12)$$

Assuming that the system is initially in a pure state given by  $\rho_S(0) = \psi(0)\psi^*(0)$ , the forward and backward stochastic wave functions can be expressed in the path integral formalism as

$$\begin{aligned} \psi(Z_\pm, t) &= \int \mathcal{D}[q^\pm] \exp \left\{ iS_0[q^\pm] - i \int_0^t ds Z_\pm(s)f(q^\pm(s)) \right. \\ &\quad \left. - \Phi_{\text{res}}[q^\pm, t] \right\} \psi(0). \quad (13) \end{aligned}$$

For practical calculation, the evolution equations of  $\psi(Z_\pm, t)$  are presented as

$$\begin{aligned} \frac{d}{dt} \psi(Z_\pm, t) &= -i \left[ \hat{H}_S + Z_\pm(t)\hat{f}(q) + \hat{f}(q) \int_0^t \right. \\ &\quad \left. \times du \tilde{\alpha}(t, u) \frac{\delta}{\delta Z_\pm(u)} \right] \psi(Z_\pm, t). \quad (14) \end{aligned}$$

The above equation shares the same structure as the NMSSE derived by Diósi and Strunz,<sup>36</sup> with two key differences: the forward and backward wave functions can be different, and there is flexibility in choosing  $\tilde{\alpha}$ , which broadens the range of applications for various temperatures and spectral densities. By solving the equations,  $\rho_S(t)$  in Eq. (2) can be obtained by averaging over an ensemble of stochastic trajectories, i.e.,  $\rho_S(t) = \mathcal{E}\{\psi(Z_+, t)\psi^*(Z_-, t)\}_z$ .

## B. HOPS and generation of noises

Dealing with the functional derivative term in Eq. (14) is challenging, but it can now be addressed using the HOPS method derived in the coherent state representation.<sup>42</sup> Alternatively, it can

be obtained by introducing auxiliary stochastic wave functions in the path integral approach.<sup>44,45</sup> By approximating the aBCF as a sum of complex exponential functions,

$$\tilde{\alpha}(t, s) \approx \sum_{k=1}^K d_k e^{-v_k(t-s)}, \quad (15)$$

and following the latter approach, we define the auxiliary wave functions as Ref. 45

$$\begin{aligned} \psi_n(Z_{\pm}, t) = & \int \mathcal{D}[q^{\pm}] \exp \left\{ iS_0[q^{\pm}] - i \int_0^t ds Z_{\pm}(s) f(q^{\pm}(s)) \right. \\ & \left. - \Phi_{\text{res}}[q^{\pm}, t] \right\} \prod_k \left[ -i \int_0^t dud_k e^{-v_k(t-u)} \right]^{n_k} \psi(0), \end{aligned} \quad (16)$$

where  $\mathbf{n} = \{n_1, n_2, \dots, n_k, \dots\}$  denotes the hierarchical order of each mode. It follows the hierarchy equations of motion,<sup>45</sup>

$$\begin{aligned} \frac{d}{dt} \psi_n(Z_{\pm}, t) = & - \left[ i\hat{H}_S + iZ_{\pm}(t)\hat{f}(q) + \sum_{k=1}^K n_k v_k \right] \psi_n(Z_{\pm}, t) \\ & + \hat{f}(q) \sum_{k=1}^K \left[ \psi_{n_k^+}(Z_{\pm}, t) - n_k d_k \psi_{n_k^-}(Z_{\pm}, t) \right], \end{aligned} \quad (17)$$

where  $\mathbf{n}_k^{\pm}$  is the shorthand for  $\mathbf{n} \pm \mathbf{e}_k$  with  $\mathbf{e}_k = \{0, 0, \dots, 1_k, \dots\}$ .

Practically, a closed form of the above equation can be obtained by choosing the terminator as  $\psi_{n_k^+} \approx \frac{\alpha(0)}{v_k} \hat{f}(q) \psi_n$  or by employing  $\psi_{n_k^+} = 0$  with an appropriate  $\mathbf{n}_k^+$ .<sup>42</sup> Consequently, Eq. (17) consists of  $\prod_{k=1}^K (n_{k,\text{max}} + 1)$  coupling equations, where  $n_{k,\text{max}}$  denotes the maximum hierarchical depth of the  $k$ th mode of Eq. (15).

The selection of the aBCF is crucial because it significantly influences the computational cost by determining the number of modes and also impacts numerical convergence. A typical scheme tailored for the high temperature case is presented as<sup>44</sup>

$$\alpha_1(t, s) = \int_0^{\infty} \frac{d\omega}{\pi} \text{csch} \frac{\beta\omega}{2} \cos \omega(t-s), \quad (18)$$

and the resulting aBCF is given by

$$\tilde{\alpha}(t, s) = \int_0^{\infty} \frac{d\omega}{\pi} J(\omega) \left[ \tanh \frac{\beta\omega}{4} \cos \omega(t-s) - i \sin \omega(t-s) \right], \quad (19)$$

where the real part decays much faster than the original BCF, especially in the high temperature case.  $Z_+$  and  $Z_-$  can be equal while satisfying Eqs. (9) and (10). After discretization of the frequency, the noise can be generated as<sup>43,44</sup>

$$\begin{aligned} Z(t) = \sum_{\lambda} \chi_{\lambda} \left[ \sqrt{\coth \frac{\beta\omega_{\lambda}}{2} + \text{csch} \frac{\beta\omega_{\lambda}}{2}} \cos(\omega_{\lambda}t + 2\pi\phi_{\lambda}) \right. \\ \left. + i \sqrt{\coth \frac{\beta\omega_{\lambda}}{2} - \text{csch} \frac{\beta\omega_{\lambda}}{2}} \sin(\omega_{\lambda}t + 2\pi\phi_{\lambda}) \right], \end{aligned} \quad (20)$$

where  $\chi_{\lambda} = \sqrt{\frac{J(\omega_{\lambda})\Delta\omega}{\pi}}$  and  $\{\phi_{\lambda}\}$  are independent random variables distributed uniformly in  $[0, 1]$ .

Alternatively, by taking  $\alpha_1(t, s) = \text{Re}\{\alpha(t, s)\}$ ,<sup>45</sup> one obtains an aBCF that exclusively incorporates the temperature-independent

imaginary component. Consequently, this decomposition leads to a reduced number of exponential function modes in Eq. (15). In particular, for the Debye spectral density

$$J(\omega) = \frac{\eta\gamma\omega}{\omega^2 + \gamma^2}, \quad (21)$$

where  $\eta$  and  $\gamma$  refer to coupling strength and characteristic frequency, respectively, the aBCF is reduced to a single exponential function,

$$\tilde{\alpha}(t, s) = -i \frac{\eta\gamma}{\pi} \int_0^{\infty} d\omega \frac{\omega}{\omega^2 + \gamma^2} \sin \omega(t-s) = -i \frac{\eta\gamma}{2} e^{-\gamma(t-s)}. \quad (22)$$

As a compromise,  $Z_+$  and  $Z_-$  are necessarily distinct, resulting in the separate evolution of stochastic wave functions on the forward and backward paths. The noises can be generated as  $Z_{\pm}(t) = Z_c(t) + \varepsilon_{\pm}(t)$ <sup>46</sup> with

$$\begin{aligned} Z_c(t) = \sum_{\lambda} \chi_{\lambda} \left[ \sqrt{\frac{n(\omega_{\lambda}) + 1}{2}} (a_{\lambda}^1 + ia_{\lambda}^2) e^{i\omega_{\lambda}t} \right. \\ \left. + \sqrt{\frac{n(\omega_{\lambda})}{2}} (a_{\lambda}^1 - ia_{\lambda}^2) e^{-i\omega_{\lambda}t} \right] \end{aligned} \quad (23)$$

and

$$\begin{aligned} \varepsilon_{\pm}(t) = \sum_{\lambda} \chi_{\lambda} \left[ \sqrt{n(\omega_{\lambda}) + 1} - \sqrt{n(\omega_{\lambda})} \right] \\ \times (b_{\pm}^1 \cos \omega_{\lambda}t + b_{\pm}^2 \sin \omega_{\lambda}t), \end{aligned} \quad (24)$$

where  $a_{\lambda}^1$ ,  $a_{\lambda}^2$ ,  $b_{\lambda,\pm}^1$ , and  $b_{\lambda,\pm}^2$  are random variables drawn from a normal distribution  $N(0, 1)$ .

In conclusion, the flexibility in choosing an aBCF broadens the range of options available when employing HOPS to address diverse scenarios.

### C. cNMSSE and its matrix product states formalism

The cNMSSE is the compact second quantization form of HOPS. It can be conveniently combined with MPS to efficiently manage the large number of auxiliary wave functions.<sup>63</sup> In the formalism of Gao *et al.*, the auxiliary wave functions in HOPS are first rescaled<sup>63,73</sup> as  $\psi_n(Z_{\pm}, t) \rightarrow (\prod_{k=1}^K n_k! |d_k|^{n_k})^{-\frac{1}{2}} \psi_n(Z_{\pm}, t)$ , and the corresponding equations of motion are reformulated as

$$\begin{aligned} \frac{d}{dt} \psi_n(Z_{\pm}, t) = & - \left[ i\hat{H}_S + iZ_{\pm}(t)\hat{f}(q) + \sum_{k=1}^K n_k v_k \right] \psi_n(Z_{\pm}, t) \\ & + \hat{f}(q) \sum_{k=1}^K \left[ \sqrt{(n_k + 1) |d_k|} \psi_{n_k^+}(Z_{\pm}, t) \right. \\ & \left. - \frac{d_k}{\sqrt{|d_k|}} \sqrt{n_k} \psi_{n_k^-}(Z_{\pm}, t) \right]. \end{aligned} \quad (25)$$

We can formally define a Fock space  $\{|\mathbf{n}\rangle\}$ , where  $|\mathbf{n}\rangle = |n_1, n_2, \dots, n_k, \dots\rangle$  encodes the hierarchical order of each mode. The states  $\{|\mathbf{n}\rangle\}$  satisfy the orthonormality condition  $\langle \mathbf{n} | \mathbf{n}' \rangle = \delta_{\mathbf{n}, \mathbf{n}'}$  and adhere to the properties of creation and annihilation

bosonic operators, defined as  $\hat{b}_k^\dagger|\mathbf{n}\rangle = \sqrt{n_k+1}|\mathbf{n}_k^+\rangle$  and  $\hat{b}_k|\mathbf{n}\rangle = \sqrt{n_k}|\mathbf{n}_k^-\rangle$ . By introducing

$$|\Psi(Z_\pm, t)\rangle = \sum_{\mathbf{n}} \psi_{\mathbf{n}}(Z_\pm, t) \otimes |\mathbf{n}\rangle, \quad (26)$$

the evolution equation of  $|\Psi(Z_\pm, t)\rangle$  can be written in a second quantization form using the aforementioned bosonic operators, referred to as cNMSSE,

$$i \frac{d}{dt} |\Psi(Z_\pm, t)\rangle = \hat{H}_{\text{eff}}(Z_\pm) |\Psi(Z_\pm, t)\rangle, \quad (27)$$

where  $\hat{H}_{\text{eff}}(Z_\pm)$  is the effective Hamiltonian determined by noises  $Z_\pm$ . By comparing the above equation with Eq. (25), we obtain the effective Hamiltonian,

$$\begin{aligned} \hat{H}_{\text{eff}}(Z_\pm) = & \hat{H}_S + \hat{f}(q) Z_\pm(t) - i \sum_{k=1}^K v_k \hat{b}_k^\dagger \hat{b}_k \\ & - i \hat{f}(q) \sum_{k=1}^K \left[ \frac{d_k}{\sqrt{|d_k|}} \hat{b}_k^\dagger - \sqrt{|d_k|} \hat{b}_k \right]. \end{aligned} \quad (28)$$

In this effective Hamiltonian, the hierarchical order  $n_k$  in HOPS is now interpreted as the occupation number of phonons with complex frequency  $v_k$ , and the states  $|\mathbf{n}\rangle$  are considered as eigenvectors within the pseudo-Fock space.

$\hat{H}_{\text{eff}}(Z_\pm)$  is in the form of sum-of-products (SOP) and thus can be conveniently represented by time-dependent matrix product operators (MPOs). By utilizing bipartite graph theory to construct the symbolic MPO containing parameters,<sup>74</sup> we can automatically generate optimal time-dependent MPOs. After expanding the auxiliary wave function on the basis of system as  $\psi_{\mathbf{n}}(Z_\pm, t) = \sum_s \psi_{\mathbf{n}}^s(Z_\pm, t) |s\rangle$ , the composite wave function is given by

$$|\Psi(Z_\pm, t)\rangle = \sum_{s, \mathbf{n}} \psi_{\mathbf{n}}^s(Z_\pm, t) |s\rangle \otimes |\mathbf{n}\rangle. \quad (29)$$

The coefficient tensor can be approximated by an MPS  $\psi_{\mathbf{n}}^s \approx \sum_a A_{1,a_1}^s A_{a_1,a_2}^{n_1} \cdots A_{a_{K-1},1}^{n_{K-1}}$ . The required stochastic wave function is  $\psi_0(Z_\pm, t) = \sum_s \psi_0^s(Z_\pm, t) |s\rangle$ . Consequently, we need to set terms

with physical index greater than zero to zero when calculating expectations,

$$\psi_0(Z_\pm, t) = \langle \mathbf{0} | \Psi(Z_\pm, t) \rangle = \sum_{s,a} A_{1,a_1}^s A_{a_1,a_2}^0 \cdots A_{a_{K-1},1}^0 |s\rangle. \quad (30)$$

### III. NUMERICAL CALCULATIONS

We applied the cNMSSE method to simulate the carrier diffusion dynamics and thereby calculate the mobility of a single carrier at various temperatures within the one-dimensional Peierls model, which features nearest-neighbor hopping and nonlocal electron-phonon interactions [Fig. 1(a)]. The Hamiltonian of the electron is given by  $\hat{H}_e = -J \sum_j (\hat{c}_j^\dagger \hat{c}_{j+1} + \hat{c}_{j+1}^\dagger \hat{c}_j)$ , where  $J$  represents the transfer integral, and the site energies are assumed to be uniform and are therefore omitted. The nonlocal phonons correspond to the intermolecular vibrational modes with their Hamiltonian expressed as  $\hat{H}_{\text{ph}} = \sum_{j,\lambda} \left( \frac{p_{j,\lambda}^2}{2} + \frac{1}{2} \omega_j^2 x_{j,\lambda}^2 \right)$ , where  $j$  denotes the pair  $\{j, j+1\}$ . Each nonlocal phonon bath is coupled linearly to the electron hopping between the adjacent sites, resulting in the off-diagonal coupling terms, i.e.,  $\hat{H}_{e\text{-ph}} = \sum_j \hat{L}_j \otimes \sum_\lambda c_\lambda \hat{x}_{j,\lambda}$  with  $\hat{L}_j = \hat{c}_j^\dagger \hat{c}_{j+1} + \hat{c}_{j+1}^\dagger \hat{c}_j$ . The resulting effective Hamiltonian in cNMSSE is presented as

$$\begin{aligned} \hat{H}_{\text{eff}}(Z_\pm) = & \hat{H}_e + \sum_j Z_{j,\pm}(t) \hat{L}_j - i \sum_{j,k} v_k \hat{b}_{j,k}^\dagger \hat{b}_{j,k} \\ & - i \sum_j \hat{L}_j \otimes \sum_k \left( \frac{d_k}{\sqrt{|d_k|}} \hat{b}_{j,k}^\dagger - \sqrt{|d_k|} \hat{b}_{j,k} \right). \end{aligned} \quad (31)$$

We assume that the carrier is initially localized at the central site of a chain consisting of 50 sites and simulate its diffusion dynamics to calculate the mean square displacement (MSD), which is defined as  $\langle [\Delta r(t)]^2 \rangle = \langle \Delta r^2(t) \rangle - \langle \Delta r(t) \rangle^2$  with

$$\langle \Delta r^2(t) \rangle = \sum_j \rho_j(t) (j - j_{\text{init}})^2 d^2, \quad (32)$$

$$\langle \Delta r(t) \rangle = \sum_j \rho_j(t) (j - j_{\text{init}}) d.$$

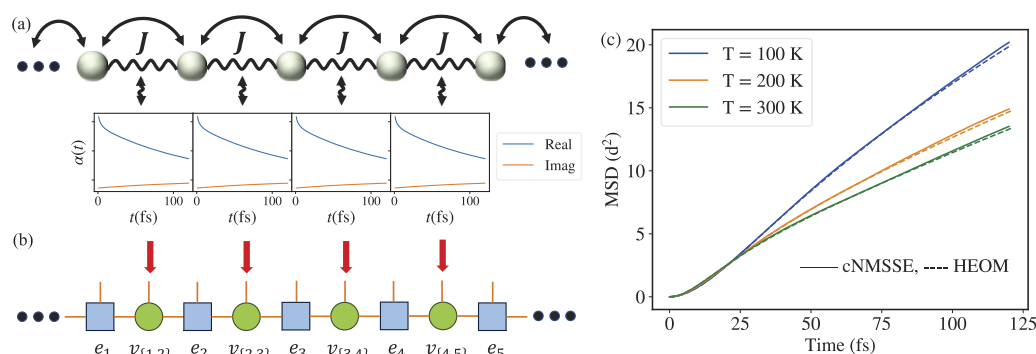


**FIG. 1.** (a) An illustrative diagram of the Peierls model. The electron-phonon interactions between neighboring sites are described by the Debye spectral density, which exhibits non-Markovian effects. (b) The MPS ansatz of the cNMSSE for the Peierls model. Each bath is decomposed into a single mode accurately. (c) The mean square displacement (MSD) of the carrier across varying temperatures. The solid lines represent results obtained from the cNMSSE method averaged over 5000 trajectories, and the dashed lines denote results from the HEOM method.

**TABLE I.** Charge carrier mobility of the Peierls model at different temperatures.

Temperature (K)	Mobility ( $\text{cm}^2 \text{V}^{-1} \text{s}^{-1}$ )	$R^2$
100	15.5	>0.999
200	5.31	>0.999
300	3.14	>0.999

Here,  $\rho_j$  represents the carrier population on site  $j$ , computed as  $\rho_j(t) = \mathcal{E}[\langle \Psi_0(Z_-, t) | \hat{N}_j | \Psi_0(Z_+, t) \rangle]$  within the forward-backward cNMSSE method. The distance  $d$  is the separation between adjacent sites. The electron-phonon interactions are described by the Debye spectral density [Eq. (21)], which manifests significant non-Markovian effects indicated by the gradual decay of the BCF [Fig. 1(a)]. Each bath is accurately decomposed into a single mode [Fig. 1(b)]. We employ the same parameters as those used by Shi *et al.*,<sup>25</sup> i.e.,  $J = 300 \text{ cm}^{-1}$ ,  $\eta = 323 \text{ cm}^{-1}$ ,  $\gamma = 41 \text{ cm}^{-1}$ , and  $d = 4 \text{ \AA}$ . The decomposition of the aBCF and the generation of noises are performed according to Eqs. (22)–(24). The time evolution is conducted by the global propagation and compression method with the fourth-order Runge-Kutta algorithm (P & C-RK4)<sup>70</sup> with the following parameters: the maximum number of phonon occupations  $n_{\text{max}} = 5$ , time step  $\Delta t = 1.0 \text{ fs}$ , and truncation threshold  $\zeta = 10^{-4}$  for MPS compression. These parameters are optimized to ensure the convergence of a single trajectory's results while minimizing computational costs (Fig. 6 in Appendix C). The results averaged over 5000 trajectories are consistent with the HEOM method, even at low temperatures (Fig. 1), verifying the reliability of the cNMSSE method.

The diffusion coefficient, defined as  $D = \lim_{t \rightarrow \infty} \frac{\langle [\Delta r(t)]^2 \rangle}{2t}$ , is determined by linear fitting of the MSD for long times. In this case, the range for linear fitting is 50–120 fs across all temperatures. Subsequently, the mobility is obtained with the formula  $\mu = eD/k_B T$ . All these findings are presented in Table I. The coefficients of determination, each exceeding 0.999, confirm that the convergence of the cNMSSE method is reliable and the carrier diffusion has reached

equilibrium. The mobility decreases with temperature, indicating the hindrance effect of nonlocal electron-phonon coupling on the carrier when the coupling strength is comparable to the transfer integral.<sup>15</sup>

We expand the parameter space to include various coupling strengths and characteristic frequencies of the phonon bath at a fixed temperature of 300 K. The results are benchmarked against the HEOM method (see Fig. 9 in Appendix D for details). Compared with the transfer integral of  $J = 300 \text{ cm}^{-1}$ , we adjust  $\eta$  to 100 and  $700 \text{ cm}^{-1}$  for weak and strong nonlocal electron-phonon interactions, respectively, with coherent diffusion dynamics ( $\eta = 0 \text{ cm}^{-1}$ ) serving as a reference. For the strong-coupling case, a larger hierarchical depth ( $n_{\text{max}} = 6$ ) and an increased number of trajectories (10 000) are required to achieve convergence (Figs. 7 and 8). The MSD curve in Fig. 2(a) illustrates that for cases with larger  $\eta$ , the MSD of the carrier increases faster initially, but slower as equilibrium is approached. Furthermore, the time required to reach equilibrium is also longer in the strong-coupling case, in contrast to the Holstein model with local electron-phonon interactions.<sup>29</sup> The impact of phonon bath frequency is investigated at  $\gamma = 10$  and  $100 \text{ cm}^{-1}$ , with 10 000 trajectories employed for the high-frequency case (Fig. 8). Generally a larger MSD is observed at higher frequencies, while the results of  $\gamma = 41$  and  $\gamma = 100 \text{ cm}^{-1}$  exhibit only minor differences within the evolutionary timeframe [Fig. 2(b)], which may be attributed to the broad distribution of the Debye spectral density [Eq. (21)].

We further evaluate the computational cost of the cNMSSE method, including both single trajectories cost and the convergence behavior. The former is gauged through the virtual bond dimension of the MPS. Figure 3 illustrates the averaged carrier population and bond dimension at varying temperatures and across several parameter regimes of phonon baths. With fixed truncation criteria of MPS compression, bond dimensions increase as the carrier diffuses and interacts with phonons. The maximum bond dimension of the averaged results exceeds 30 at the bond corresponding to the mid-point site and diminishes to nearly zero at about 30 bonds away from the center, coinciding with sites where the population approaches zero. In Figs. 3(a)–3(c), we observe that although the carrier tends to

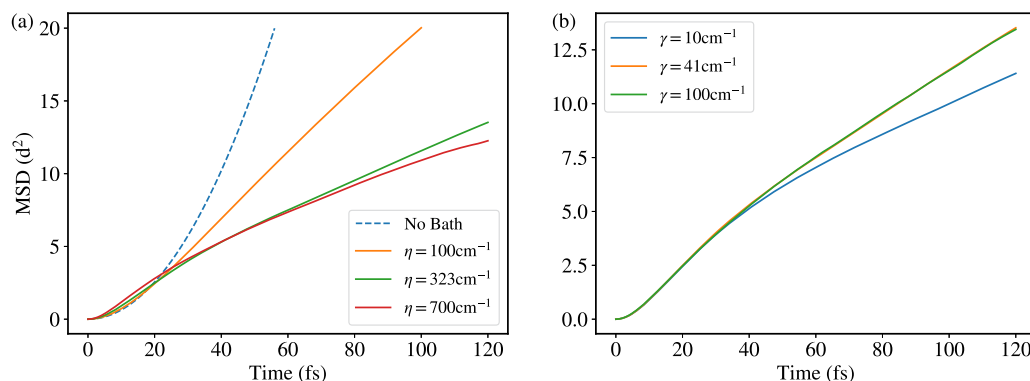


**FIG. 2.** MSD of the carrier at various coupling strengths and characteristic frequencies. From the default parameter set, i.e.,  $\eta = 323 \text{ cm}^{-1}$ ,  $\gamma = 41 \text{ cm}^{-1}$ ,  $J = 300 \text{ cm}^{-1}$ , and  $T = 300 \text{ K}$ , we change  $\eta$  to 100 and  $700 \text{ cm}^{-1}$  in (a) and change  $\gamma$  to 10 and  $100 \text{ cm}^{-1}$  in (b). All results are averaged over 5000 trajectories except for  $\eta = 700 \text{ cm}^{-1}$  and  $\gamma = 100 \text{ cm}^{-1}$ , which are averaged over 10 000 trajectories.

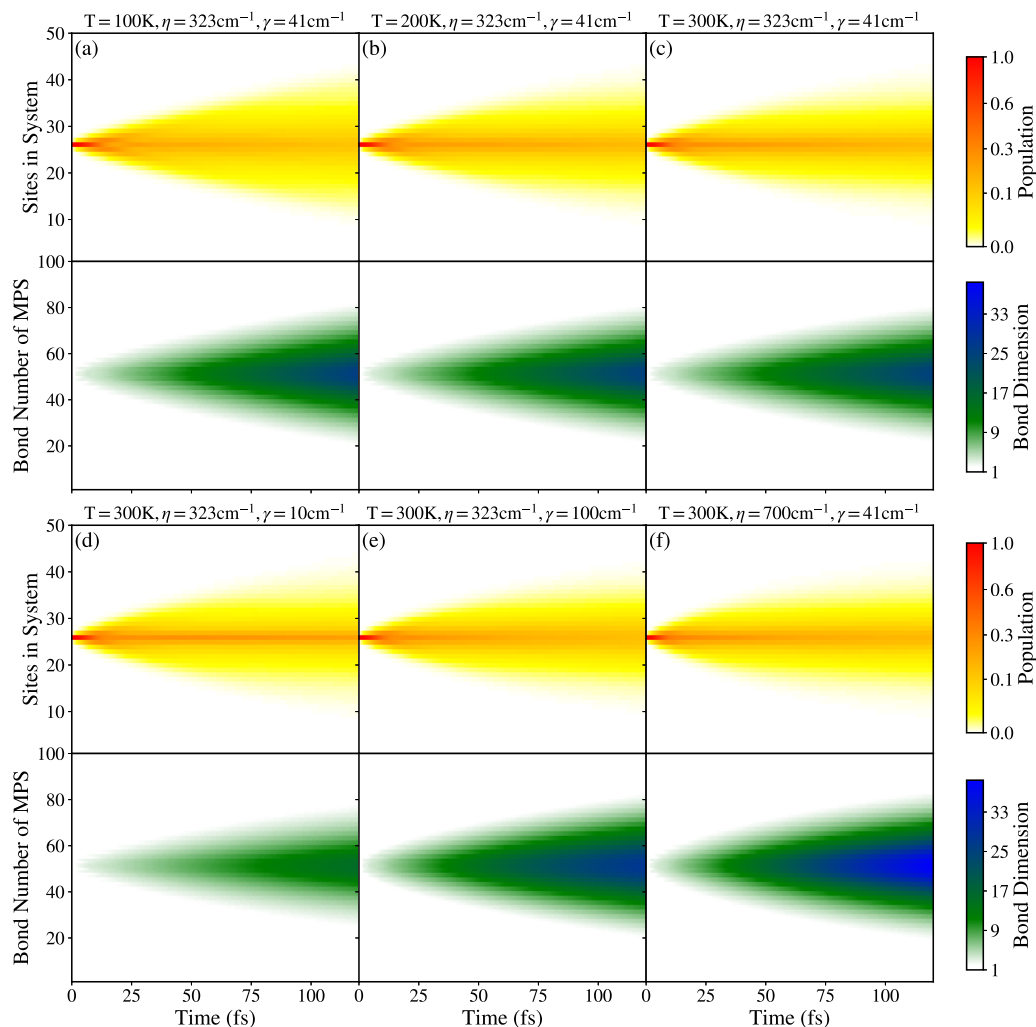


**FIG. 3.** Carrier population dynamics and virtual bond dimensions of MPS for various sets of parameters. (a)–(c) Differences across various temperatures, (c)–(e) indicate alterations resulting from different characteristics frequencies, and (c) and (f) variations between intermediate and strong coupling strengths.

localize with increasing temperature, the temperature dependence of bond dimension is not obvious. The averaged bond dimension increases with increasing coupling strength  $\eta$  or characteristic frequency  $\gamma$ , as shown in Figs. 3(c)–3(f). To gain a more intuitive insight into the computational cost, we record the average time cost required per trajectory for system sizes ranging from 30 to 100 sites, across different coupling strengths (Fig. 4). The computational time increases in the strong coupling regime, in agreement with the trend of the rising bond dimension. Moreover, we observe that for larger systems, the time cost scales linearly to the system size, while for smaller systems, the time cost is somewhat larger compared to the linear scaling observed in larger systems. The critical number of sites at which this transition occurs is found to increase with the strength of the coupling.

Finally, we evaluated the convergence of cNMSSE by determining the standard errors of  $\langle \Delta r^2(t) \rangle$ ,

$$\sigma_N(t) = \sqrt{\frac{\sum_{j=1}^N (x_j - \bar{x})^2}{N(N-1)}}, \quad x = \langle \Delta r^2(t) \rangle, \quad (33)$$

since the value  $\langle \Delta r(t) \rangle$  is nearly negligible and contributes little to the MSD.  $N$  denotes the number of trajectories. The results were averaged over 200, 1000, and 5000 trajectories for temperatures 100 and 300 K, as well as the strong-coupling and high-frequency cases. As depicted in Fig. 8 in Appendix D, the standard errors decrease as the number of trajectories increases, confirming the convergence of the cNMSSE method. The standard errors at 100 K are larger than those at higher temperatures, in line with the greater stability of the forward-backward cNMSSE method at higher temperatures.<sup>45</sup> Strong electron-phonon interactions and high-frequency phonon baths also lead to larger standard errors, requiring more trajectories to achieve convergence and enhance the linearity of the MSD.

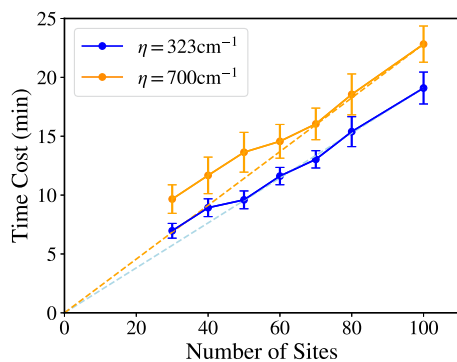


**FIG. 4.** Average time cost per trajectory, calculated over 50 trajectories, for systems of varying sizes. The dashed lines indicate the low scaling of the computational time with the system size. The calculations were performed on a four-core, 8 GB RAM virtual machine with Intel Xeon Platinum 8255C CPU @ 2.50 GHz.

#### IV. CONCLUSION

In this work, we integrate the forward-backward formalism of noise generation with the cNMSSE method to investigate the charge transport process in organic semiconductors with nonlocal electron-phonon interactions. Although two stochastic wave functions evolve separately, the resulting aBCF consists solely of the temperature-independent imaginary part, simplifying the decomposition process and enhancing accuracy. As a result, the nonlocal electron-phonon interaction, characterized by the Debye spectral density, can be precisely decomposed into a single complex mode. We apply the forward-backward cNMSSE method to examine carrier diffusion dynamics in the one-dimensional Peierls model and calculate the mobility at varying temperatures and across phonon baths with various coupling strengths and characteristic frequencies. The reliability of our method is validated by benchmarking against the HEOM method. The cost of computing single trajectories and the convergence behavior both highlight the efficiency of the cNMSSE method. Moreover, the computational time for single trajectories exhibits low scaling with respect to system size.

This forward-backward cNMSSE holds potential for further extension and broader developments. Phonon baths characterized by a low temperature, high frequency, and strong coupling might result in numerical instabilities and difficulties in achieving convergence, posing a significant challenge to both cNMSSE and HEOM methods.<sup>75–77</sup> The utilization of the localized nature of carriers by combining the cNMSSE method with the adHOPS method may help us achieve a size-invariant cNMSSE method.<sup>49,51</sup> The flexibility in selecting noise generation and BCF decomposition schemes encourages the use of the cNMSSE method to explore different temperatures and various types of spectral densities. The MPS/MPO representation of the pure state and Hamiltonian in cNMSSE can also be adapted to more flexible topological structures of tensor networks, such as tree tensor network states and operators.<sup>62</sup> The successful application of the HOPS + MPS to the Holstein-Hubbard model<sup>64,78</sup> has motivated us to further investigate both electron-phonon and electron-electron interactions in open quantum dynamics. Due to its wave function nature and compatibility with TNS, the cNMSSE

method is a promising tool for the study of non-Markovian quantum dynamics for large open quantum systems.

#### ACKNOWLEDGMENTS

This work was supported by the National Natural Science Foundation of China (Grant Nos. T2350009 and 22273122), the Guangdong Provincial Natural Science Foundation (Grant Nos. 2024A1515011185 and 2024A1515011504), and the Shenzhen city “Pengcheng Peacock” Talent Program. Liqi Zhou expresses gratitude to Qiang Shi’s group for their assistance with the HEOM method program used for benchmarking and to Jiajun Ren for his help with the Renormalizer package.

#### AUTHOR DECLARATIONS

##### Conflict of Interest

The authors have no conflicts to disclose.

#### Author Contributions

**Liqi Zhou:** Conceptualization (equal); Data curation (equal); Formal analysis (equal); Investigation (equal); Methodology (supporting); Software (equal); Validation (equal); Visualization (lead); Writing – original draft (lead); Writing – review & editing (equal). **Xing Gao:** Conceptualization (equal); Data curation (equal); Formal analysis (equal); Investigation (equal); Methodology (lead); Project administration (supporting); Software (equal); Supervision (equal); Validation (equal); Visualization (supporting); Writing – review & editing (equal). **Zhigang Shuai:** Conceptualization (supporting); Funding acquisition (lead); Project administration (lead); Supervision (equal); Validation (equal); Writing – review & editing (equal).

#### DATA AVAILABILITY

The data that support the findings of this study are available from the corresponding authors upon reasonable request.

#### APPENDIX A: THE RENORMALIZER PACKAGE

We implement the cNMSSE method on Renormalizer, a python package based on tensor network states for electron-phonon quantum dynamics.<sup>79</sup> Previously, Renormalizer was primarily exploited to study the full quantum dynamics of systems with significant electron-phonon interaction.<sup>14,15,69</sup> It can be readily extended to open quantum dynamics methods utilizing effective Hamiltonians in the sum-of-products (SOP) form, such as the cNMSSE. The architecture of Renormalizer, described in Fig. 5, has the following features:

- The latest version of Renormalizer has supported the construction of both MPS and tree tensor network states (TTNS). It automatically and analytically constructs optimal Matrix Product Operators (MPOs) and Tree Tensor Network Operators (TTNOs) for operators in SOP form,

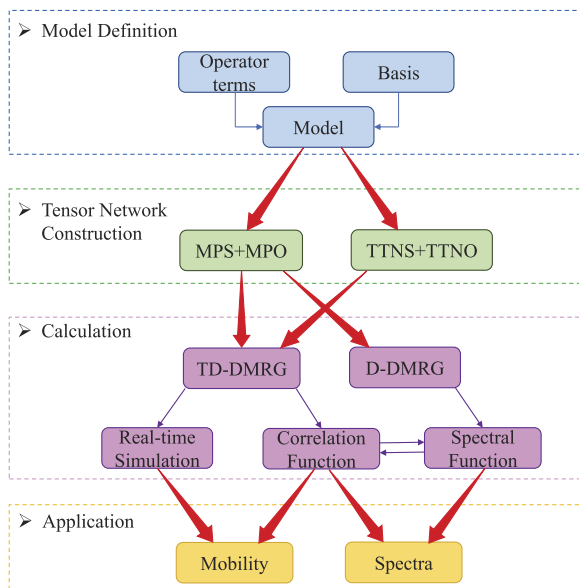


FIG. 5. Architecture of Renormalizer.

utilizing bipartite graph theory.<sup>74,80</sup> Renormalizer also supports parameterized operators and MPOs, enabling efficient handling of time-dependent Hamiltonians. The MPS can be initialized in various forms, such as a Hartree-product state, or an entangled state. The exact ground state can then be achieved through static DMRG optimization. In addition, users can conduct imaginary-time propagation for ground states or thermal equilibrium states.

- The calculation module offers a comprehensive framework for both time-dependent DMRG and dynamical DMRG<sup>81</sup> at both zero and finite temperatures. Various time evolution schemes are supported, including the traditional

propagation and progress (P & C) method and the state-of-art time-dependent variational principle (TDVP) method.<sup>70</sup> During DMRG sweeping for both ground-state optimization and time evolution, the On-the-Fly Swapping (OFS) algorithm can optimize the sorting of degrees of freedom.<sup>82</sup> Graphics processing unit (GPU) acceleration with Cupy as backend is also supported.<sup>70</sup>

- Utilizing the previously mentioned algorithms, Renormalizer offers modules to calculate the spectra and charge transfer properties of organic materials.

## APPENDIX B: THE HUBBARD-STRAONOVICH TRANSFORMATION OF THE INFLUENCE FUNCTIONAL

The H-S transformation represents the inverse application of the multi-dimensional Gaussian integral of complex variables.<sup>83</sup> This transformation begins with the calculation of the characteristic function,

$$\kappa(\mathbf{k}) = \frac{1}{C} \int d\mathbf{z} e^{-\frac{1}{2}\mathbf{z}^T \Phi \mathbf{z} + i\mathbf{k}^T \mathbf{z}}, \quad (\text{B1})$$

where  $\mathbf{z} = (z_1, z_2, \dots, z_i, \dots)$  is a complex vector with  $z_i = (z_i, z_i^*)$  and  $\mathbf{k}$  is a complex vector sharing the same dimension as  $\mathbf{z}$ . The Gaussian kernel matrix  $\Phi$  is normalized by the coefficient  $C$  and satisfies

$$\Phi_{ij}^{-1} = \begin{pmatrix} \langle z_i z_j \rangle & \langle z_i z_j^* \rangle \\ \langle z_i^* z_j \rangle & \langle z_i^* z_j^* \rangle \end{pmatrix}. \quad (\text{B2})$$

Equation (B1) can be simplified by completing the square as follows:

$$\begin{aligned} \kappa(\mathbf{k}) &= \frac{1}{C} \int d\mathbf{z} e^{-\underbrace{(z-i\Phi^{-1}\mathbf{k})^T \Phi (z-i\Phi^{-1}\mathbf{k})}_{1}} e^{-\frac{1}{2}\mathbf{k}^T \Phi^{-1} \mathbf{k}} \\ &= e^{-\frac{1}{2}\mathbf{k}^T \Phi^{-1} \mathbf{k}}, \end{aligned} \quad (\text{B3})$$

which can be written in a more detailed form,

$$\left\langle \exp \left[ i \sum_i (k_i z_i + k'_i z_i^*) \right] \right\rangle = \exp \left\{ -\frac{1}{2} \sum_{ij} \begin{pmatrix} k_i & k'_i \end{pmatrix} \begin{pmatrix} \langle z_i z_j \rangle & \langle z_i z_j^* \rangle \\ \langle z_i^* z_j \rangle & \langle z_i^* z_j^* \rangle \end{pmatrix} \begin{pmatrix} k_j \\ k'_j \end{pmatrix} \right\}. \quad (\text{B4})$$

Upon taking the continuous limit by treating the index  $i, j$  as time  $s, u$ , we derive the relation of Gaussian noise  $Z(t)$ ,

$$\begin{aligned} &\mathcal{E} \left\{ \exp \left[ i \int_0^t ds (k(s)Z(s) + k'(s)Z^*(s)) \right] \right\}_z \\ &= \exp \left\{ -\frac{1}{2} \int_0^t ds \int_0^t du \begin{pmatrix} k(s) & k'(s) \end{pmatrix} \begin{pmatrix} \mathcal{E}\{Z(s)Z(u)\}_z & \mathcal{E}\{Z(s)Z^*(u)\}_z \\ \mathcal{E}\{Z^*(s)Z(u)\}_z & \mathcal{E}\{Z^*(s)Z^*(u)\}_z \end{pmatrix} \begin{pmatrix} k(u) \\ k'(u) \end{pmatrix} \right\} \\ &= \exp \left\{ -\int_0^t ds \int_0^s du \begin{pmatrix} k(s) & k'(s) \end{pmatrix} \begin{pmatrix} \mathcal{E}\{Z(s)Z(u)\}_z & \mathcal{E}\{Z(s)Z^*(u)\}_z \\ \mathcal{E}\{Z^*(s)Z(u)\}_z & \mathcal{E}\{Z^*(s)Z^*(u)\}_z \end{pmatrix} \begin{pmatrix} k(u) \\ k'(u) \end{pmatrix} \right\}. \end{aligned} \quad (\text{B5})$$

Equation (B5) can be naturally generalized to the multi-noise case,

$$\begin{aligned} & \mathcal{E} \left\{ \exp \left[ i \int_0^t ds \sum_i (k_i(s) Z_i(s) + k'_i(s) Z_i^*(s)) \right] \right\}_z \\ &= \exp \left\{ - \int_0^t ds \int_0^s du \sum_{ij} (k_i(s) k'_j(s)) \begin{pmatrix} \mathcal{E} \{ Z_i(s) Z_j(u) \}_z & \mathcal{E} \{ Z_i(s) Z_j^*(u) \}_z \\ \mathcal{E} \{ Z_i^*(s) Z_j(u) \}_z & \mathcal{E} \{ Z_i^*(s) Z_j^*(u) \}_z \end{pmatrix} \begin{pmatrix} k_i(u) \\ k'_j(u) \end{pmatrix} \right\}. \end{aligned} \quad (\text{B6})$$

For the case of two noises,  $Z_+$  and  $Z_-$ , by setting  $k_+(s) = -f(q^+(s))$ ,  $k'_-(s) = f(q^-(s))$ , and  $k_-(s) = k'_+(s) = 0$ , we can simplify Eqs. (B6) to (7).

### APPENDIX C: THE OPTIMIZATION OF PARAMETERS

The parameters that affect the accuracy of an individual trajectory include the maximum number of phonon occupations  $n_{\max}$ , the time step  $\Delta t$ , and the truncation threshold  $\zeta$  for MPS compression. By applying a fixed noise, we can evaluate the  $\langle \Delta r^2(t) \rangle$  and  $\langle \Delta r(t) \rangle$  of the single trajectory as we vary the parameter values. The parameters are considered determined once the results reach convergence.  $n_{\max}$  dictating the maximum hierarchical depth of the

HOPS method is crucial for determining the accuracy of the method and was therefore optimized first. With the default time step  $\Delta t = 1.0$  fs and truncation threshold  $\zeta = 10^{-4}$ , Figs. 6(a)–6(f) demonstrate that  $n_{\max} = 5$  is sufficient to ensure the convergence of the result across all temperatures.

Subsequently, we optimized  $\Delta t$  and  $\zeta$  concurrently, as they collectively influence the accuracy of the P&C-RK4 method.<sup>70</sup> Lowering the truncation threshold during compression can indeed improve the accuracy, whereas the effect of decreasing the time step is distinct. Reducing  $\Delta t$  increases the number of evolution steps, leading to more compressions and potential error amplification. This issue becomes particularly significant with large  $\zeta$  and small  $\Delta t$ , where the truncation error might exceed the actual change of

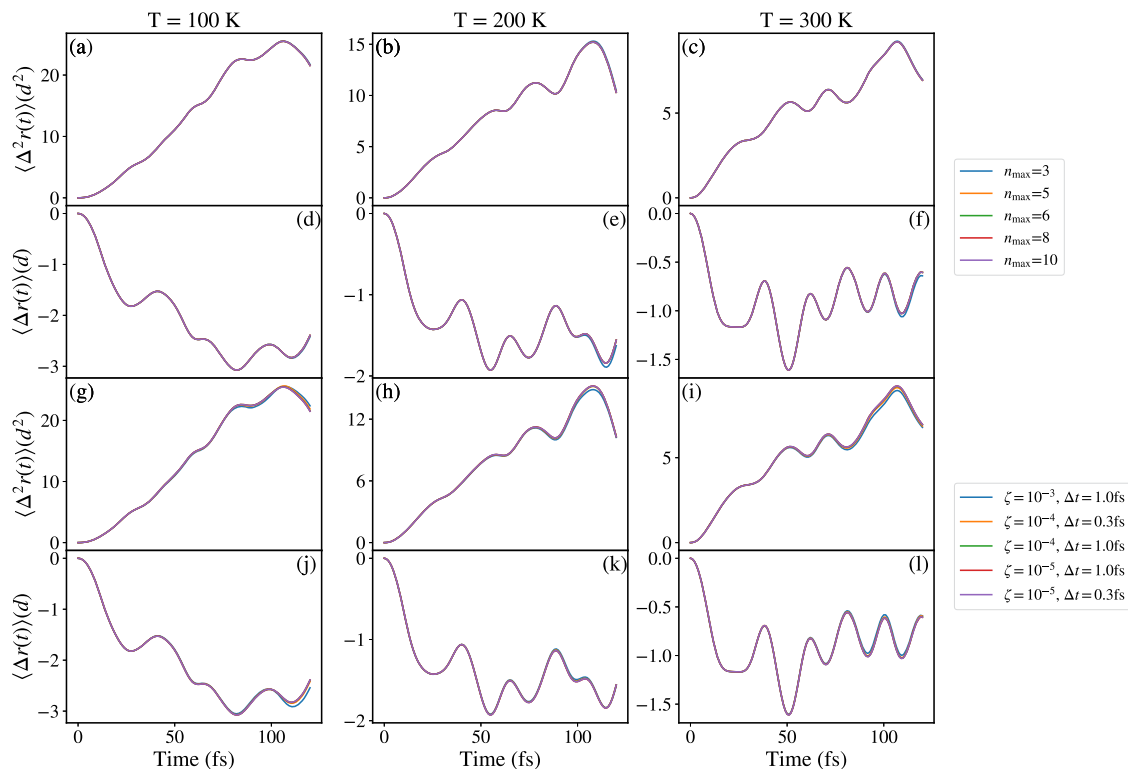


**FIG. 6.** Parameter optimization via single-trajectory convergence assessment across diverse temperature conditions. (a)–(f) Optimization of the maximum number of phonon occupations  $n_{\max}$  with the default time step  $\Delta t = 1.0$  fs and truncation threshold  $\zeta = 10^{-4}$ . In (g)–(l), we optimize the time step  $\Delta t$  and truncation threshold  $\zeta$  with the optimized  $n_{\max} = 5$ .

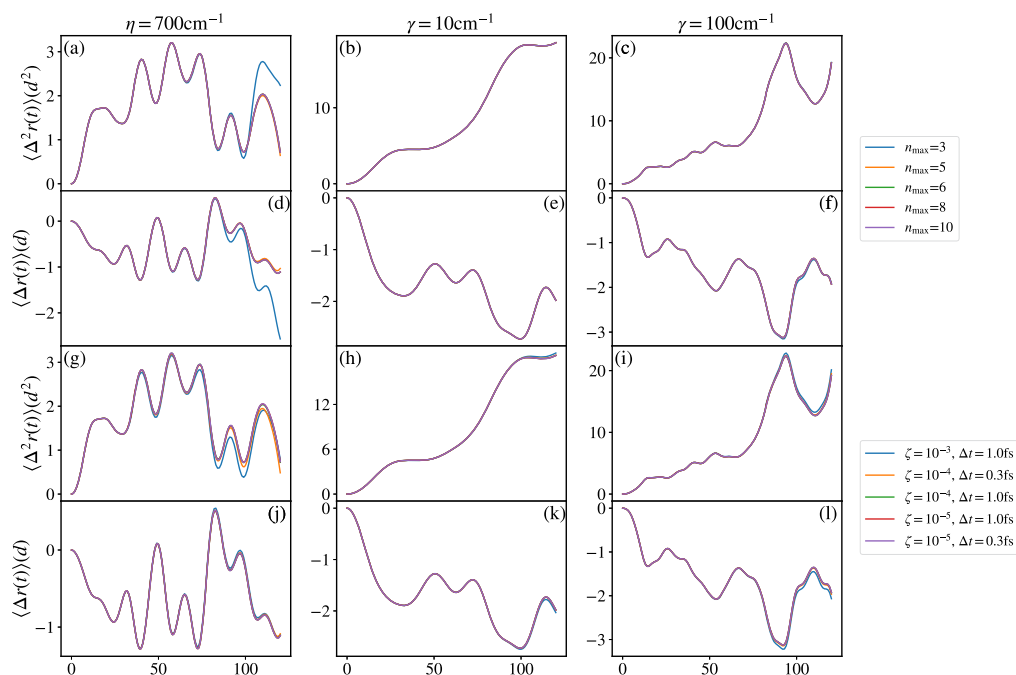


**FIG. 7.** Parameter optimization via single-trajectory convergence assessment for phonon baths with varying coupling strengths and characteristic frequencies. We follow the same procedure applied in Fig. 6. The title for each column indicates the differences in parameters from the default set, i.e.,  $\eta = 323 \text{ cm}^{-1}$ ,  $\gamma = 41 \text{ cm}^{-1}$ , and  $T = 300 \text{ K}$ .

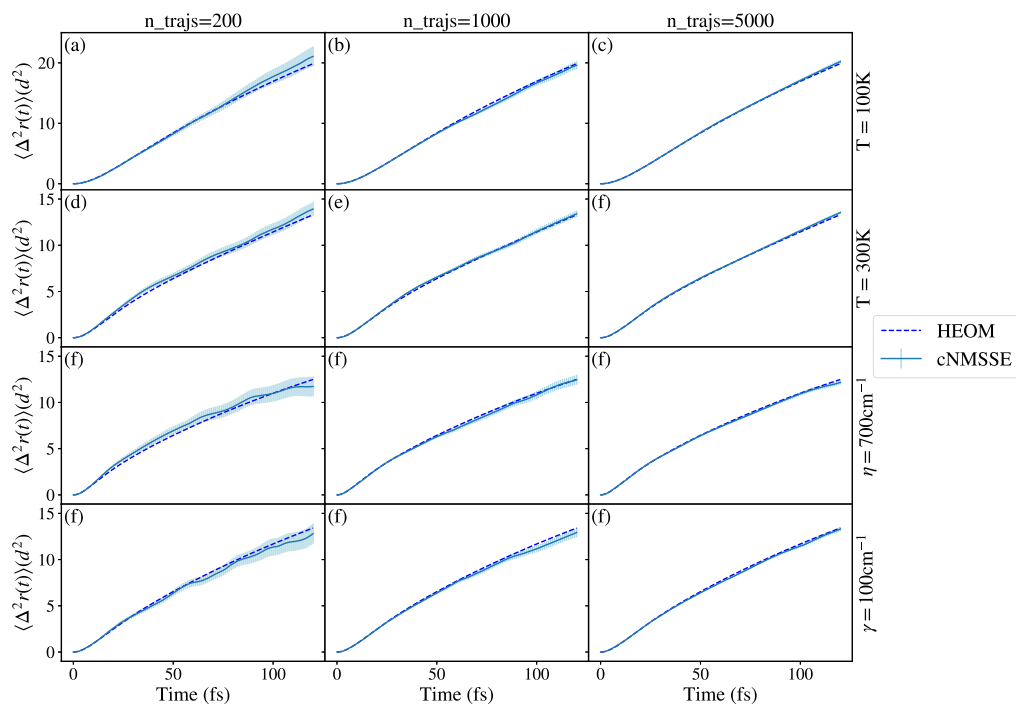


**FIG. 8.** Convergence assessment of the cNMSSE method for the Peierls model at different temperatures by evaluating the standard errors of  $\langle \Delta^2 r(t) \rangle$ . Each row corresponds to a certain set of parameters, while each column corresponds to results averaged over 200, 1000, and 5000 trajectories, respectively. The label for each row indicates the differences in parameters from the default set, i.e.,  $\eta = 323 \text{ cm}^{-1}$ ,  $\gamma = 41 \text{ cm}^{-1}$ , and  $T = 300 \text{ K}$ .

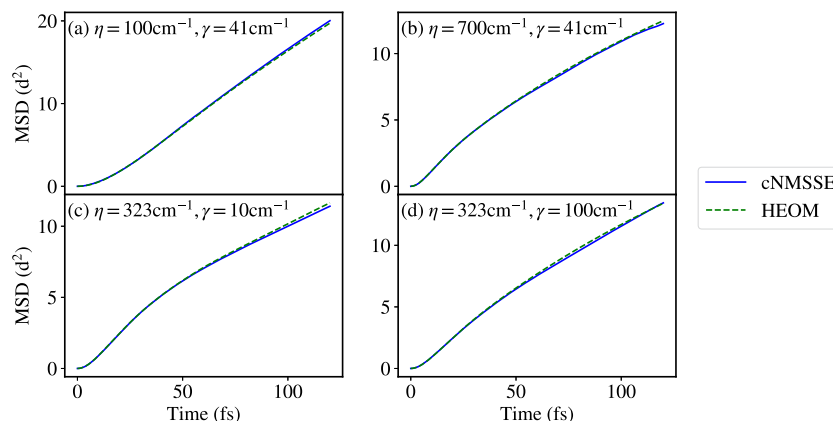


FIG. 9. MSD of the carrier across varying coupling strengths  $\eta$  and characteristic frequencies  $\gamma$  at 300 K, which are benchmarked against the HEOM method.

the MPS at each step. Consequently, accuracy is not necessarily enhanced by merely reducing the time step. With the optimized parameter  $n_{\max} = 5$ , we confirmed that  $\Delta t = 1.0$  fs and  $\zeta = 10^{-4}$  are adequate for convergence. In contrast, the case with  $\Delta t = 0.3$  fs and  $\zeta = 10^{-4}$  demonstrates the potential for error amplification [Figs. 6(g)–6(l)].

Parameters are optimized for different coupling strengths  $\eta$  and characteristic frequencies  $\gamma$  as well, as depicted in Fig. 7. For the strong coupling case with  $\eta = 700$  cm $^{-1}$ , a larger  $n_{\max}$  is required for the convergence of a single trajectory, whereas different characteristic frequencies do not necessitate an increased hierarchical depth. The optimized time step and truncation threshold remain consistent across different parameter sets.

#### APPENDIX D: CONVERGENCE BEHAVIOR OF MULTIPLE TRAJECTORIES

The convergence of the cNMSSE method is also assessed by calculating the standard errors of  $\langle \Delta r^2(t) \rangle$ , as given in Eq. (33). The standard errors diminish with increasing trajectories, indicating the convergent behavior of the cNMSSE method (Fig. 8). However, in case of strong coupling and high-frequency phonon baths, the linearity of the curves is not as apparent as in the other cases, which requires more trajectories to reach convergence.

We compare the results of the cNMSSE method with those of the HEOM method as complement to Fig. 2. The MSD curves are obtained by averaging over 5000 trajectories for the weak-coupling and low-frequency cases and over 10 000 trajectories for the strong coupling and high-frequency cases.

#### REFERENCES

- <sup>1</sup>V. Coropceanu, J. Cornil, D. A. da Silva Filho, Y. Olivier, R. Silbey, and J.-L. Brédas, *Chem. Rev.* **107**, 926 (2007).
- <sup>2</sup>T. Nematiram and A. Troisi, *J. Chem. Phys.* **152**, 190902 (2020).
- <sup>3</sup>O. H. LeBlanc, Jr., *J. Chem. Phys.* **35**, 1275 (1961).
- <sup>4</sup>L. Tang, M. Long, D. Wang, and Z. Shuai, *Sci. China, Ser. B: Chem.* **52**, 1646 (2009).

- <sup>5</sup>B. Blükle, A. Troisi, R. Häusermann, and B. Batlogg, *Phys. Rev. B* **93**, 035205 (2016).
- <sup>6</sup>H. Bässler, *Phys. Status Solidi B* **175**, 15 (1993).
- <sup>7</sup>G. Nan, X. Yang, L. Wang, Z. Shuai, and Y. Zhao, *Phys. Rev. B* **79**, 115203 (2009).
- <sup>8</sup>R. Munn and R. Silbey, *J. Chem. Phys.* **83**, 1854 (1985).
- <sup>9</sup>K. Hannewald and P. Bobbert, *Phys. Rev. B* **69**, 075212 (2004).
- <sup>10</sup>S. Ciuchi, S. Fratini, and D. Mayou, *Phys. Rev. B* **83**, 081202 (2011).
- <sup>11</sup>S. Fratini, D. Mayou, and S. Ciuchi, *Adv. Funct. Mater.* **26**, 2292 (2016).
- <sup>12</sup>H. Oberhofer, K. Reuter, and J. Blumberger, *Chem. Rev.* **117**, 10319 (2017).
- <sup>13</sup>S. Giannini, A. Carof, and J. Blumberger, *J. Phys. Chem. Lett.* **9**, 3116 (2018).
- <sup>14</sup>W. Li, J. Ren, and Z. Shuai, *J. Phys. Chem. Lett.* **11**, 4930 (2020).
- <sup>15</sup>W. Li, J. Ren, and Z. Shuai, *Nat. Commun.* **12**, 4260 (2021).
- <sup>16</sup>V. May and O. Kühn, *Charge and Energy Transfer Dynamics in Molecular Systems* (John Wiley and Sons, 2023).
- <sup>17</sup>I. De Vega and D. Alonso, *Rev. Mod. Phys.* **89**, 015001 (2017).
- <sup>18</sup>X. Xie, A. Santana-Bonilla, and A. Troisi, *J. Chem. Theory Comput.* **14**, 3752 (2018).
- <sup>19</sup>N. Makri and D. E. Makarov, *J. Chem. Phys.* **102**, 4600 (1995).
- <sup>20</sup>N. Makri and D. E. Makarov, *J. Chem. Phys.* **102**, 4611 (1995).
- <sup>21</sup>Y. Tanimura and R. Kubo, *J. Phys. Soc. Jpn.* **58**, 101 (1989).
- <sup>22</sup>Y. Tanimura, *J. Chem. Phys.* **153**, 020901 (2020).
- <sup>23</sup>S. Nakajima, *Prog. Theor. Phys.* **20**, 948 (1958).
- <sup>24</sup>R. Zwanzig, *J. Chem. Phys.* **33**, 1338 (1960).
- <sup>25</sup>D. Wang, L. Chen, R. Zheng, L. Wang, and Q. Shi, *J. Chem. Phys.* **132**, 081101 (2010).
- <sup>26</sup>L. Chen, Y. Zhao, and Y. Tanimura, *J. Phys. Chem. Lett.* **6**, 3110 (2015).
- <sup>27</sup>L. Song and Q. Shi, *J. Chem. Phys.* **142**, 174103 (2015).
- <sup>28</sup>Y. Yan, M. Xu, Y. Liu, and Q. Shi, *J. Chem. Phys.* **150**, 234101 (2019).
- <sup>29</sup>T. Li, Y. Yan, and Q. Shi, *J. Chem. Phys.* **160**, 111102 (2024).
- <sup>30</sup>J. Shao, *J. Chem. Phys.* **120**, 5053 (2004).
- <sup>31</sup>J. T. Stockburger, *Chem. Phys.* **296**, 159 (2004).
- <sup>32</sup>Y. Tanimura, *J. Phys. Soc. Jpn.* **75**, 082001 (2006).
- <sup>33</sup>C.-Y. Hsieh and J. Cao, *J. Chem. Phys.* **148**, 014103 (2018).
- <sup>34</sup>C.-Y. Hsieh and J. Cao, *J. Chem. Phys.* **148**, 014104 (2018).
- <sup>35</sup>J. M. Moix and J. Cao, *J. Chem. Phys.* **139**, 134106 (2013).
- <sup>36</sup>L. Diósi and W. T. Strunz, *Phys. Lett. A* **235**, 569 (1997).
- <sup>37</sup>L. Diósi, N. Gisin, and W. T. Strunz, *Phys. Rev. A* **58**, 1699 (1998).
- <sup>38</sup>J. T. Stockburger and H. Grabert, *Phys. Rev. Lett.* **88**, 170407 (2002).
- <sup>39</sup>X. Zhong and Y. Zhao, *J. Chem. Phys.* **135**, 134110 (2011).
- <sup>40</sup>L. Han, Y. Ke, X. Zhong, and Y. Zhao, *Int. J. Quantum Chem.* **115**, 578 (2015).
- <sup>41</sup>Y. Jiang, Z. Shuai, and M. Liu, *J. Phys. Chem. C* **122**, 18365 (2018).

- <sup>42</sup>D. Suess, A. Eisfeld, and W. Strunz, *Phys. Rev. Lett.* **113**, 150403 (2014).
- <sup>43</sup>X. Zhong and Y. Zhao, *J. Chem. Phys.* **138**, 014111 (2013).
- <sup>44</sup>K. Song, L. Song, and Q. Shi, *J. Chem. Phys.* **144**, 224105 (2016).
- <sup>45</sup>Y. Ke and Y. Zhao, *J. Chem. Phys.* **145**, 024101 (2016).
- <sup>46</sup>Y. Ke and Y. Zhao, *J. Chem. Phys.* **147**, 184103 (2017).
- <sup>47</sup>M. Lian, Y.-C. Wang, Y. Ke, and Y. Zhao, *J. Chem. Phys.* **151**, 044115 (2019).
- <sup>48</sup>L. Chen, D. I. G. Bennett, and A. Eisfeld, *J. Chem. Phys.* **156**, 124109 (2022).
- <sup>49</sup>L. Varvelo, J. K. Lynd, and D. I. G. Bennett, *Chem. Sci.* **12**, 9704 (2021).
- <sup>50</sup>T. Gera, L. Chen, A. Eisfeld, J. R. Reimers, E. J. Taffet, and D. I. G. B. Raccach, *J. Chem. Phys.* **158**, 174103 (2023).
- <sup>51</sup>B. Citty, J. K. Lynd, T. Gera, L. Varvelo, and D. I. G. B. Raccach, *J. Chem. Phys.* **160**, 144118 (2024).
- <sup>52</sup>U. Schollwöck, *Ann. Phys.* **326**, 96 (2011).
- <sup>53</sup>H. Ma, Z. Luo, and Y. Yao, *Mol. Phys.* **116**, 854 (2018).
- <sup>54</sup>J. Ren, W. Li, T. Jiang, Y. Wang, and Z. Shuai, *Wiley Interdiscip. Rev.: Comput. Mol. Sci.* **12**, e1614 (2022).
- <sup>55</sup>E. Ye and G. K. Chan, *J. Chem. Phys.* **155**, 044104 (2021).
- <sup>56</sup>M. R. Jørgensen and F. A. Pollock, *Phys. Rev. Lett.* **123**, 240602 (2019).
- <sup>57</sup>M. Cygorek, J. Keeling, B. W. Lovett, and E. M. Gauger, *Phys. Rev. X* **14**, 011010 (2024).
- <sup>58</sup>A. Strathearn, P. Kirton, D. Kilda, J. Keeling, and B. W. Lovett, *Nat. Commun.* **9**, 3322 (2018).
- <sup>59</sup>Q. Shi, Y. Xu, Y. Yan, and M. Xu, *J. Chem. Phys.* **148**, 174102 (2018).
- <sup>60</sup>R. Borrelli, *J. Chem. Phys.* **150**, 234102 (2019).
- <sup>61</sup>Y. Ke, R. Borrelli, and M. Thoss, *J. Chem. Phys.* **156**, 194102 (2022).
- <sup>62</sup>Y. Ke, *J. Chem. Phys.* **158**, 211102 (2023).
- <sup>63</sup>X. Gao, J. Ren, A. Eisfeld, and Z. Shuai, *Phys. Rev. A* **105**, L030202 (2022).
- <sup>64</sup>S. Flannigan, F. Damanet, and A. J. Daley, *Phys. Rev. Lett.* **128**, 063601 (2022).
- <sup>65</sup>A. Troisi and G. Orlandi, *Phys. Rev. Lett.* **96**, 086601 (2006).
- <sup>66</sup>L. Wang and D. Beljonne, *J. Phys. Chem. Lett.* **4**, 1888 (2013).
- <sup>67</sup>L. Wang and D. Beljonne, *J. Chem. Phys.* **139**, 064316 (2013).
- <sup>68</sup>R. Munn and R. Silbey, *J. Chem. Phys.* **83**, 1843 (1985).
- <sup>69</sup>J. Ren, Z. Shuai, and G. Kin-Lic Chan, *J. Chem. Theory Comput.* **14**, 5027 (2018).
- <sup>70</sup>W. Li, J. Ren, and Z. Shuai, *J. Chem. Phys.* **152**, 024127 (2020).
- <sup>71</sup>R. Feynman and F. Vernon, *Ann. Phys.* **24**, 118 (1963).
- <sup>72</sup>J. Hubbard, *Phys. Rev. Lett.* **3**, 77 (1959).
- <sup>73</sup>Q. Shi, L. Chen, G. Nan, R.-X. Xu, and Y. Yan, *J. Chem. Phys.* **130**, 164518 (2009).
- <sup>74</sup>J. Ren, W. Li, T. Jiang, and Z. Shuai, *J. Chem. Phys.* **153**, 084118 (2020).
- <sup>75</sup>A. Ishizaki and Y. Tanimura, *J. Phys. Soc. Jpn.* **74**, 3131 (2005).
- <sup>76</sup>Y. Yan, T. Xing, and Q. Shi, *J. Chem. Phys.* **153**, 204109 (2020).
- <sup>77</sup>T. P. Fay, *J. Chem. Phys.* **157**, 054108 (2022).
- <sup>78</sup>M. Moroder, M. Grundner, F. Damanet, U. Schollwöck, S. Mardazad, S. Flannigan, T. Köhler, and S. Paeckel, *Phys. Rev. B* **107**, 214310 (2023).
- <sup>79</sup>“Renormalizer 0.1.0 documentation—shuaigroup.github.io,” <https://shuaigroup.github.io/Renormalizer/index.html>.
- <sup>80</sup>W. Li, J. Ren, H. Yang, H. Wang, and Z. Shuai, “Optimal tree tensor network operators for tensor network simulations: Applications to open quantum systems,” *J. Chem. Phys.*, **161**, 054116 (2024); [arXiv:2407.13098](https://arxiv.org/abs/2407.13098).
- <sup>81</sup>T. Jiang, W. Li, J. Ren, and Z. Shuai, *J. Phys. Chem. Lett.* **11**, 3761 (2020).
- <sup>82</sup>W. Li, J. Ren, H. Yang, and Z. Shuai, *J. Phys.: Condens. Matter* **34**, 254003 (2022).
- <sup>83</sup>G. M. G. McCaul, “Stochastic representations of open systems,” Ph.D. thesis, King’s College, London, 2019.